Available online at www.sciencedirect.com

ScienceDirect

Ceramics International 39 (2013) 9125–9136

CERAMICS INTERNATIONAL

www.elsevier.com/locate/ceramint

Diethylene glycol mediated synthesis of Gd_2O_3:Eu^{3+} nanophosphor and its Judd–Ofelt analysis

R.G. Abhilash Kumar[a], Satoshi Hata[b], K.G. Gopchandran[a,*]

[a]Department of Optoelectronics, University of Kerala, Thiruvananthapuram 695581, India
[b]Department of Electrical and Materials Science, Faculty of Engineering Sciences, Kyushu University, Kasuga, Fukuoka 816-8580, Japan

Received 20 April 2013; accepted 3 May 2013
Available online 14 May 2013

Abstract

$Gd_{1.9}Eu_{0.1}O_3$ nanophosphor with enhanced photoemission is successfully synthesized by a controlled combustion method of metal–citrate complex in diethylene glycol medium. It is found that the phase formation and spectral properties including quantum efficiency are highly sensitive to sintering temperature and the role of citric acid both as a chelating agent and as a fuel for combustion was evident in the study. The formation of cubic Gd_2O_3:Eu nanocrystalline phosphor was confirmed by X-ray diffraction, Raman and Infrared measurements. Transmission electron microscopic images together with the SAED patterns indicate the formation of spherical Gd_2O_3 nanocrystalline powder with well defined planes separated by 0.312 nm of cubic Gd_2O_3. The high degrees of homogeneity observed in the electron micrographs are attributed to the glycol medium used. The intensities of transitions between different J levels depend on the symmetry of the local environment of Eu^{3+} activators and are described using the Judd–Ofelt analysis. The spectral properties of the samples prepared under optimum conditions have shown large asymmetric ratio, indicating high degree of distortion in local environment around Eu^{3+} ions and a maximum quantum efficiency of 78% was obtained. The life-time measurements indicated an increase from 0.83 to 1.28 ms with increase in sintering temperature from 700 to 1000 °C. The chromaticity and correlated colour temperature of the emission were evaluated based on the 1931 CIE chromaticity diagram. The absorptions observed in the excitation spectra show the suitability of the nanophosphor obtained in this study for getting excited in UV, NUV and visible regions for a variety of device applications.
© 2013 Elsevier Ltd and Techna Group S.r.l. All rights reserved.

Keywords: A. Powders: chemical preparation; A. Sintering; B. Spectroscopy; C. Lifetime; Gd_2O_3

1. Introduction

Controlled synthesis of ultrafine particles or nanoparticles might have great potential for use in solid state functional materials and devices, especially phosphors, sensors, catalysts, drug delivery carriers, etc. [1]. Phosphors represent the class of inorganic crystal structures capable of emitting radiation in visible and/or ultraviolet region as a result of excitation by an external source like electron or photon beam [2,3]. Over the past several years, there has been an ongoing search for nanometer structured phosphors with superior characteristics over their micrometer counterparts. It is anticipated that the advent of nanosized phosphors could lead not only to improved resolution in devices but also lead to an increase in luminescent efficiency. Now research in the realms of nanocrystalline phosphors extends band gap semiconductors to lanthanide doped insulators. Rare earth oxides have been widely used in high performance luminescent devices, opto-electronic devices, sensors, magnets, and other functional devices due to the unique optical, electronic, magnetic, and chemical properties arising from their 4f–5d electron transition and spin configuration [4]. Similar to Y_2O_3, Gd_2O_3 is a typical rare earth sesquioxide phosphor material for hosting trivalent activator ions. Advantages of Gd_2O_3 include high density, favourable chemical durability, thermal stability and low phonon energy. Gadolinium oxide doped with Eu^{3+} ions (Gd_2O_3:Eu^{3+}) is a red emitting phosphor that has been widely used in fluorescent lamps, white light emitting diodes, flat-panel displays, plasma display panels, field emission

*Corresponding author. Tel.: +91 47 1230 8167.
E-mail address: gopchandran@yahoo.com (K.G. Gopchandran).

0272-8842/$ - see front matter © 2013 Elsevier Ltd and Techna Group S.r.l. All rights reserved.
http://dx.doi.org/10.1016/j.ceramint.2013.05.010

displays, cathode-ray tubes, etc. [5]. Recently, Eu^{3+}:Gd_2O_3 nanoparticles received more attention due to the potential biological and germicidal applications [6,7]. Nowadays, deep UV LEDs with the emission wavelengths in the UV-B (280–315 nm) and UV-C (180–280 nm) regions of the electromagnetic spectrum have been developed to fabricate the tri-band based white LEDs. These UV-B and UV-C based white LEDs are potentially used in medical applications. Hence high-quality phosphors operating under UV excitation are needed for better performance of these LEDs [8]. The Eu^{3+} ions substitute the Gd^{3+} ions in Gd_2O_3:Eu^{3+} and occupy the lattice sites C_2 and S_6 in the cubic phase. Eu^{3+} doped Gd_2O_3 nanocrystals have shown rich luminescent features due to the possible paths of activating the trivalent rare-earth ion, Eu^{3+} through different sensitization processes, by the host Gd_2O_3 absorption, Eu–O charge transfer, the Gd^{3+} ion absorption, and the Eu^{3+} ion self excitation. The initial state has usually the same parity as the final one. However, the $4f^n$ transitions leading to luminescence were experimentally observed for Eu^{3+} ions in Gd_2O_3:Eu^{3+} nanocrystals. The mixture of opposite-parity state configurations, for example, the $4f^{n-1}5d$ and charge transfer states should make these transitions partially allowed.

For successful application in various devices, phosphor particles should be non-aggregated with fine size, narrow size distribution and spherical morphology. The spherical shape of the particles aids their dense packing and reduces light scattering from the surface. The properties such as emission lifetime, quantum efficiency, and concentration quenching depend on size of the particles [9,10]. Chemical synthesis routes, like co-precipitation, sol–gel, hydrothermal, and combustion methods, or synthesis through aerosol, offer many advantages over conventional procedures for nanoscaled materials processing. Since the precursors are mixed at the molecular level in a solution high degree of structural homogeneity is achievable; doping is effective; surface area of powder produced is very high, leading to lower processing temperature for synthesis. Up to now, various rare earth doped Gd_2O_3 phosphors in various morphologies such as spheres, plates, rods, nanotubes, nanowires, 3D flowers, and thin films have been synthesized by a variety of techniques such as sol–gel methods, aerosol routes, co-precipitation methods, molten salt routes, chemical vapour deposition, pulsed laser deposition, hydrogen flame pyrolysis methods, non-hydrolytic high temperature methods, combustion methods, spray pyrolysis and hydrothermal routines [11–22].

This paper reports a cost effective route to synthesize spherical shaped $Gd_{1.9}Eu_{0.1}O_3$ nanophosphors through the controlled combustion of metal–citrate complex. In this process, citric acid acts as a chelating agent to metal cations via the hydroxyl and carboxyl groups. The polymerizing ability of citric acid is effectively utilized for the formation of metal–citrate complex, where the metal ions are uniformly distributed. Apart from this, citric acid performed also as a fuel and caused controlled exothermic reactions with nitrates resulting in the formation of highly luminescent $Gd_{1.9}Eu_{0.1}O_3$ nanophosphors. Attempts have also been made to optimize the sintering temperature to obtain samples with enhanced luminescent properties.

2. Experimental

Materials employed for synthesis were gadolinium oxide (Gd_2O_3, 99.99%, Aldrich), europium oxide (Eu_2O_3, 99.99%, Aldrich), conc. HNO_3 (70%, Merck), polyethylene glycol 200 (PEG, 99%, Merck), diethylene glycol (DEG, $C_4H_{10}O_3$, Merck, 99%) and citric acid monohydrate ($C_6H_8O_7 \cdot H_2O$, A.R. grade). Stoichiometric amounts of Eu_2O_3 and Gd_2O_3 corresponding to the composition $Gd_{1.9}Eu_{0.1}O_3$ were dissolved in concentrated nitric acid and deionized water ($1HNO_3$:$1H_2O$) to make their respective nitrate solutions. The two solutions were then mixed under magnetic stirring to assure uniform mixing and citric acid in DEG was added slowly into the prepared aqueous nitrate solution to chelate metal ions to form metal–citrate complex. The molar ratio of citric acid to metal nitrates was fixed at 2:1. About 2 ml of PEG is also added to this solution as a mineraliser. The mixed solution was then maintained at ~100 °C with continuous stirring in a water bath until a highly transparent viscous solution is obtained. The resulting viscous solution is then put in a muffle furnace at 180 °C for 1 h to aid gelation and is then subjected to combustion at 400 °C to obtain the greyish precursor. The precursor powders thus obtained are fully ground and were then subjected to sintering in a muffle furnace at various temperatures from 500 to 1000 °C for 2 h at a heating rate of 4 °C/min to obtain the Eu^{3+} doped Gd_2O_3 nanophosphors.

The crystal structure and phase analysis of the samples were done using an X-ray diffractometer (Philips PANalytical X'Pert Pro) operating at 40 kV and 40 mA with Cu Kα radiation (λ=1.54056 Å) in the angular range (2θ) from 10° to 60° employing an X'Celerator and a monochromator at the diffracted beam side. Phase identification of the samples was performed using the X'Pert Highscore Software in support with the ICDD-PDF2 database. Low and high resolution transmission electron microscopy (TEM) were performed using a FEI Tecnai F20 electron microscope with a field emission gun operating at 200 KV. For TEM observations, the samples were prepared by dispersing the samples ultrasonically in ethanol and dried them by dropping onto a carbon coated copper grid. The infrared (IR) spectra of the samples were recorded in the range 400–4000 cm^{-1} on a Fourier transform infrared (FTIR) spectrometer (Shimadzu IRPrestige-21) using the KBr pellet method. The diffuse reflectance (DRS) measurements were carried out on a UV–vis spectrophotometer (JASCO V550) equipped with an integrating sphere (ISV-469) attachment and $BaSO_4$ is used as the reference for measurements to evaluate their band gaps. The Raman spectra of all samples were recorded in backscattering geometry using a (Horiba Jobin-Yvon LABRAM-HR800) confocal laser microRaman spectrometer system equipped with a semiconductor diode laser having 785 nm emission (operated at a current of 198 mA) and employing a peltier cooled CCD detector. A Jobin-Yvon Horiba Fluorolog (FL3-11) spectrofluorometer equipped with a 450 W Xenon lamp as excitation source and a photomultiplier tube in the photon counting mode (Hamamatsu R928P) as detector is employed to record the excitation and emission photoluminescence spectra at room temperature. The lifetime

measurements were recorded by decay by the delay method with a FL-1040 phosphorimeter attachment to spectrofluorometer employing a microsecond pulsed Xenon lamp as the source of excitation. The CIE colour coordinates (x, y) and correlated colour temperature (CCT) of the nanophosphors were calculated from the photoluminescent emission spectra based on the 1931 CIE 2 degree colour matching functions. All the measurements were done at room temperature. Judd–Ofelt and radiative parameters of the synthesized phosphor materials were determined from the photoluminescent emission spectra and life time data.

3. Results and discussion

3.1. Phase, structure and morphology studies

Fig. 1 shows the powder X-ray diffraction (XRD) patterns of $Gd_{1.9}Eu_{0.1}O_3$ nanophosphor prepared at different temperatures. Phase formation was not complete for phosphors synthesized at low temperatures lower than 700 °C and contained carbonaceous impurities. All the peaks in the diffraction pattern are indexed according to JCPDS data of cubic Gd_2O_3 (JCPDS File no. 12-0797, Ia3 (206) space group). No peaks from other phases coupled with the dopant were detected, implying that the samples are of high purity and Eu^{3+} has been uniformly incorporated into the host lattice of Gd_2O_3 by substitution. It is observed that the intensity of XRD peaks increase and width of peaks decrease with increase of sintering temperature. This indicates an improvement of crystallinity and increase in grain size with increase of sintering temperature. The lattice constant (a) of the prepared phosphors were calculated from the lattice spacing (d) of the hkl crystal planes according to the equation of cubic crystal system given by

$$\frac{1}{d^2} = \frac{(h^2 + k^2 + l^2)}{a^2} \quad (1)$$

The calculated lattice constants, cell volume and their deviations in values of the samples are summarized in

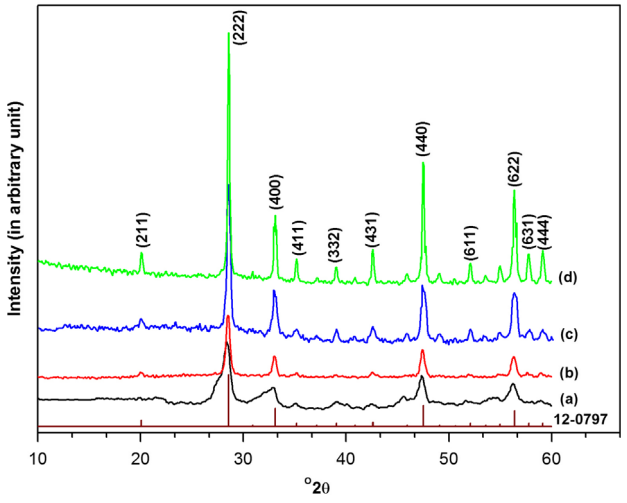

Fig. 1. XRD patterns of $Gd_{1.9}Eu_{0.1}O_3$ nanophosphors prepared at different sintering temperatures (a) 700, (b) 800, (c) 900 and 1000 °C.

Table 1
Unit cell constants, deviations and grain size of the synthesized $Gd_{1.9}Eu_{0.1}O_3$ nanophosphors.

Temperature (°C)	Lattice constant (a)/ deviation (Å)	Cell volume/ deviation (Å)^3	Grain size (nm)
JCPDS 12-0797	10.813	1264.266	–
700	10.86053 (0.04753)	1281.012 (16.746)	11.04
800	10.82547 (0.01247)	1268.646 (4.380)	17.2474
900	10.82035 (0.007346)	1266.845 (2.579)	27.738
1000	10.81794 (0.004942)	1266.001 (1.735)	39.28

Table 1, along with the standard data (JCPDS no. 12-0797) of cubic Gd_2O_3. The obtained change in lattice constant can be attributed to the nanocrystalline nature of the samples and slight differences in ionic radius of europium and gadolinium. The crystallite size of the samples is given in Table 1, calculated from XRD patterns using the Debye–Scherrer equation:

$$\text{Crystallite size } (D_{hkl}) = \frac{K\lambda}{\beta_{hkl}\cos\theta_{hkl}} \quad (2)$$

where K is a constant (=0.9), λ is the wavelength of X-rays (0.154056 nm), β is the diffracted full width at half maximum (FWHM) in radian, θ is the Bragg diffraction angle and D_{hkl} represents the size along the (hkl) direction. The average crystallite sizes of the samples were calculated from the four XRD peaks (222), (400), (440) and (622).

Fig. 2(a) and (b) presents the typical TEM images of $Gd_{1.9}Eu_{0.1}O_3$ nanophosphor prepared at 800 °C for 2 h. TEM images show that the nanoparticles are almost uniform size with rounded edges. The size of these nanoparticles obtained from the TEM images is found to be 25 ± 2 nm and is in consistent with the value calculated from X-ray diffraction pattern. It is well known that spherical shaped grains are of greater importance because of their high packing density, lower scattering of light and better luminescence properties [23] for display applications. Fig. 2(c) and (d) is the corresponding HRTEM image and the selected area electron diffraction (SAED) pattern. HRTEM image shows the highly nanocrystalline nature of the samples with well defined interplanar spacing of 0.312 nm, in accordance with the preferentially oriented plane observed in the X-ray diffraction pattern.

3.2. Optical studies

The band gap (E_g) of the samples can be deduced from the UV–vis diffuse reflectance spectra in which the Kubelka–Munk function ($F(R_\infty)$) was used to convert the reflectance of the sample (R_{sample}), normalized by the reflectance of the reference ($R_{reference}$), into an equivalent absorption spectrum. The Kubelka–Munk treatment can be written as [24,25]

$$\frac{K}{S} = \frac{(1-R_\infty)^2}{2R_\infty} \equiv F(R_\infty) \quad (3)$$

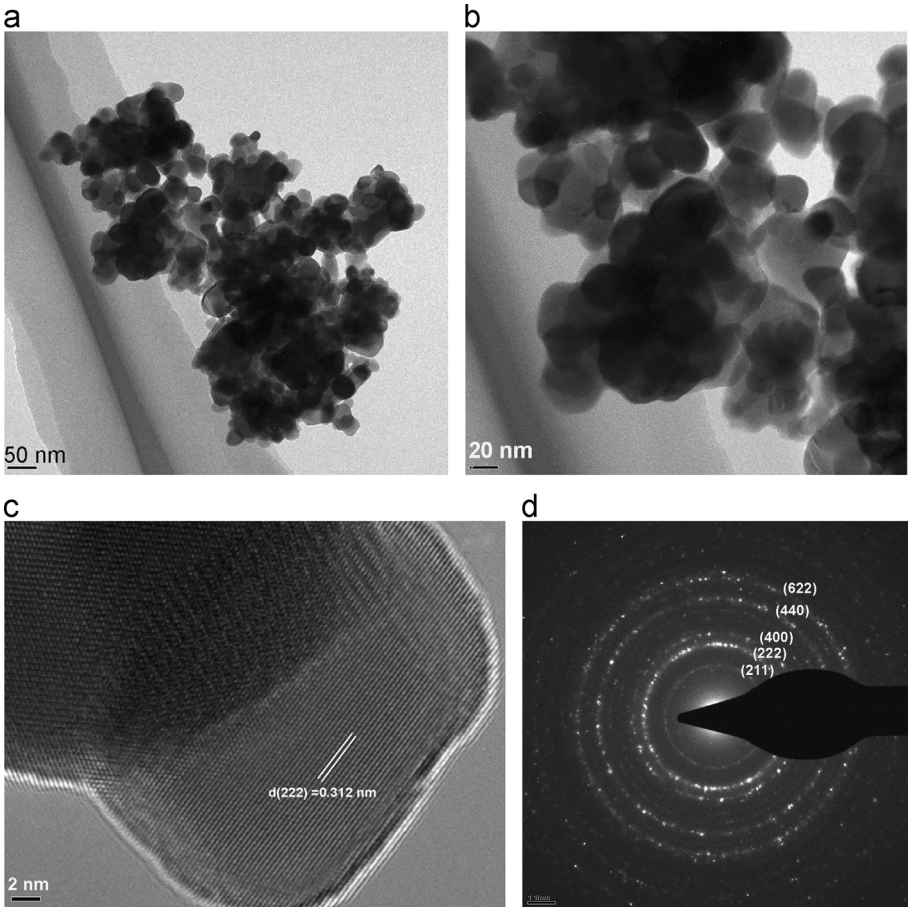

Fig. 2. (a)–(c) TEM images and (d) SAED pattern of the $Gd_{1.9}Eu_{0.1}O_3$ sample sintered at 800 °C.

$$F(R_\infty)h\upsilon \propto (h\upsilon - E_g)^n \quad (4)$$

where $R_\infty = R_{sample}/R_{reference}$, '$K$' is the absorption coefficient and 'S' is the scattering coefficient, $h\upsilon$ is the energy of the incident photon and the exponent, n depends on the type of optical transition caused by the photon absorption. In this study, n was chosen for the best fit to 1/2, indicating a direct-allowed optical transition. The scattering coefficients are weakly dependent on the energy, and thus $F(R_\infty)$ can be assumed to be proportional to the absorption coefficient within the narrow energy range containing the absorption edge features. Fig. 3 shows the plot of square of the Kubelka–Munk function multiplied by the photon energy as a function of the photon energy. The band gap energy of the prepared nanophosphors was found to be in the range 5.65–5.68 eV with respect to the sintering temperature. It can be noted that the estimated band gap energy of all the samples is higher than the band gap energy value of bulk Gd_2O_3 (5.44 eV) probably due to the confinement effect of charge carriers in these small particles.

Fig. 4 shows the FTIR transmission spectra of $Gd_{1.9}Eu_{0.1}O_3$ nanophosphors prepared at different temperatures. The absorption band around 3420 cm^{-1} can be attributed to the stretching vibration mode of O–H which provide evidence of water of hydration in the structure or may be due to surface adsorbed water from atmosphere [26,27]. For low temperature synthesized samples, the presence of carbonate ions is indicated by the appearance of absorption doublets in the region 1350–1600 cm^{-1}($\nu 3$ of CO_3^{2-}, around 1410 and 1521 cm^{-1}), $\nu 1$ of CO_3^{2-} around 1080 cm^{-1} and also by the occurrence of multiple absorptions ranging from 500 to 1000 cm^{-1} ($\nu 2$ and $\nu 4$ of CO_3^{2-}) [26–28]. As the sintering temperature increases, these vibrations vanish resulting in high purity samples. The bands around 544 and 440 cm^{-1} are assigned to the typical Gd–O vibration of cubic Gd_2O_3 [29], and the intensity of this vibrational band is found to increase with increase in sintering temperature, indicating increase of crystallinity.

The microRaman spectrum of $Gd_{1.9}Eu_{0.1}O_3$ samples measured with 785 nm laser line is shown in Fig. 5 (the spectra were normalized to the most intense band and are shifted in the y-axis for clarity) and was used to characterize the phonon energy. Gd_2O_3 is a C-type RE sesquioxide (isostructural to Y_2O_3) body centred cubic with space group Ia3, Th^7, $Z=16$ [30]. The structure contains 32 cations and 48 anions. Two kinds of cations exist: 8 RE^{3+} ions are on the b-sites with symmetry S_6 and 24 RE^{3+} ions on the d-sites with point symmetry C_2 while the 48 oxygen are on the e-sites with point symmetry C_1 [30,31]. Since the structure is body-centred, the unit cell contains the primitive structure twice, so that eight unit formulas can be used to theoretically determine the number of vibrations. The irreducible

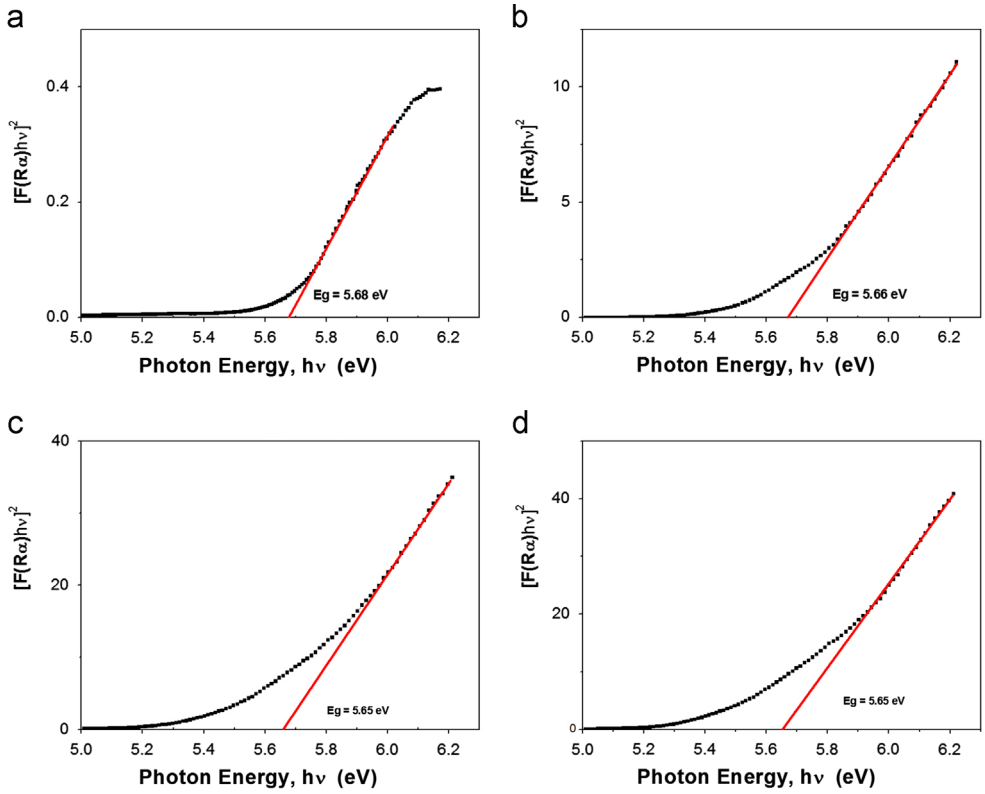

Fig. 3. Kubelka–Munk $[(F(R\alpha)h\nu)^2$ vs. photon energy] plots of the $Gd_{1.9}Eu_{0.1}O_3$ nanophosphors. (a) 700 °C, (b) 800 °C, (c) 900 °C and (d) 1000 °C.

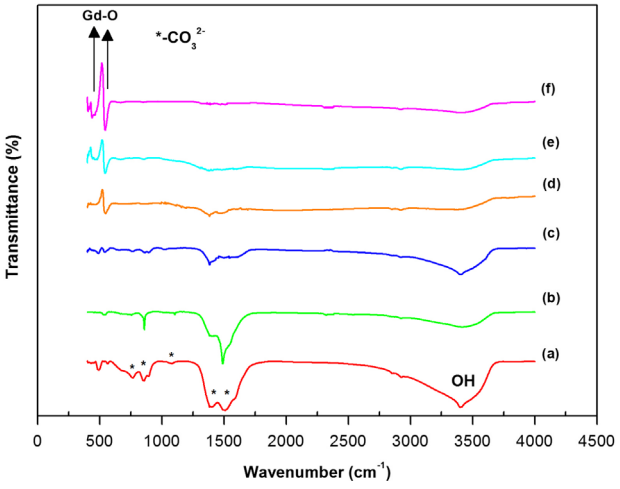

Fig. 4. FTIR spectra of $Gd_{1.9}Eu_{0.1}O_3$ nanophosphors prepared at different sintering temperatures (a) 500, (b) 600, (c) 700, (d) 800, (e) 900 and (f) 1000 °C.

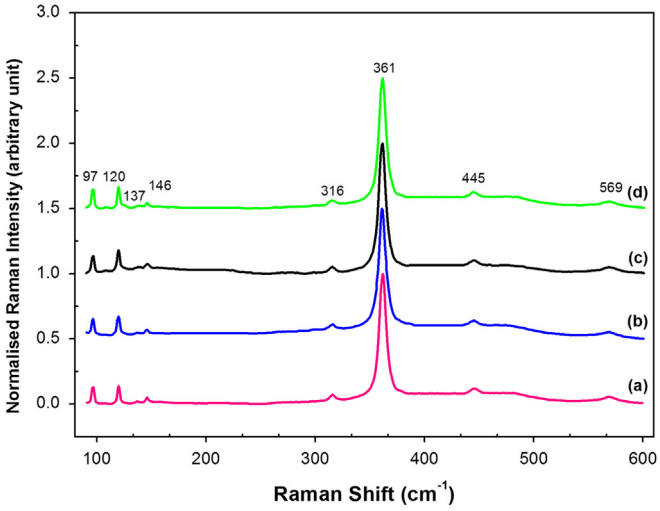

Fig. 5. Normalized Raman spectra of $Gd_{1.9}Eu_{0.1}O_3$ nanophosphors synthesized at (a) 700, (b) 800, (c) 900 and (d) 1000 °C.

representations for the optical and acoustical modes [31,32] are as below

$$\Gamma_{op} = 4A_g + 4E_g + 14F_g + 5A_{2u} + 5E_u + 16F_u, \quad \Gamma_{ac} = F_u \tag{5}$$

where A_g, E_g, and F_g are the Raman active, F_u is the infrared active and A_{2u} and E_u are inactive. Thus by the factor group analysis, 22 Raman modes have been predicted for the C-type bixbyite structured rare-earth sesquioxide, Gd_2O_3. Out of these $4A_g$, $4E_g$ and $14F_g$ are the Raman active. The samples showed Raman peaks around several bands located at 97, 120, 135, 145, 316, 361, 445 and 569 cm^{-1} corresponding to cubic Gd_2O_3 [33] and no significant change in the position of Raman peaks is observed in the spectrum. The intense band at 361 cm^{-1} corresponds to F_g+A_g mode of vibration, having large polarizability change [33].

3.3. Luminescent, Judd–Ofelt and radiative analysis

Fig. 6 shows the photoluminescence excitation (PLE) spectrum of $Gd_{1.9}Eu_{0.1}O_3$ phosphor synthesized at 800 °C by

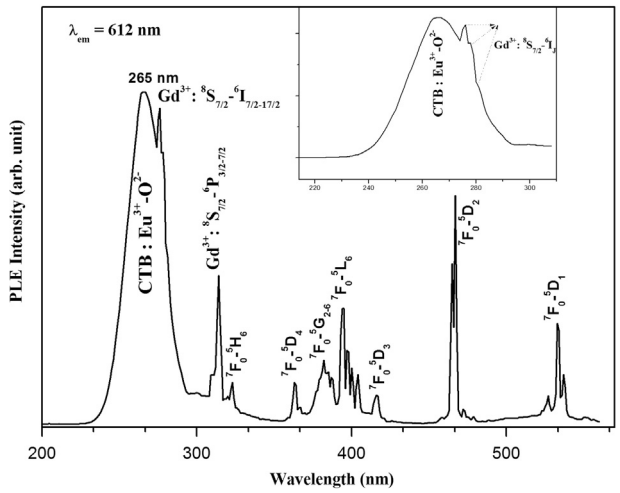

Fig. 6. Excitation spectrum of $Gd_{1.9}Eu_{0.1}O_3$ nanophosphor synthesized at 800 °C (inset shows the expanded view of the emission spectrum in the wavelength range 200–300 nm).

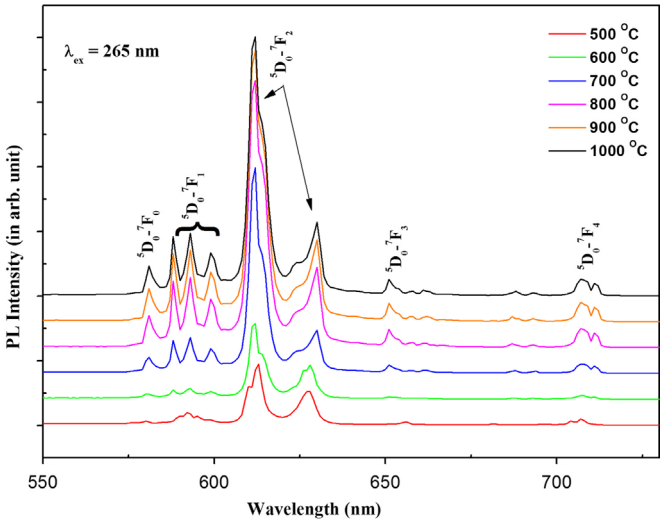

Fig. 7. Emission spectra of $Gd_{1.9}Eu_{0.1}O_3$ nanophosphors synthesized at different temperatures under CTB excitation (λ_{ex} = 265 nm).

monitoring the emission wavelength at 612 nm (λ_{em} = 612 nm). The excitation spectrum consists of a strong broad band in the wavelength range 220–300 nm with a maximum at 265 nm and is due to the charge transfer (CT) electronic transition from the 2p orbital of O^{2-} to the empty 4f orbital of central Eu^{3+} ions [5] depending on the covalency between O^{2-} and Eu^{3+}, bond volume polarization, charge of the ligand in the chemical bond and coordination number of central Eu^{3+} ion [34–36]. Weak lines observed at 276, 279, 280 ($^8S_{7/2}$–$^6I_{7/2–17/2}$) and 314 nm ($^8S_{7/2}$–$^6P_{3/2–7/2}$) are related to internal f–f transitions of Gd^{3+} ion. The presence of these lines in the excitation spectrum indicates efficient energy transfer from Gd^{3+} to Eu^{3+} in the sample [37]. Sharp lines above 320 nm belong to the intrinsic f–f transitions of Eu^{3+} within its $4f^6$ configurations, assigned to the electronic transitions of $^7F_0$–$^5H_6$ at 323 nm, $^7F_0$–$^5D_4$ at 364 nm, $^7F_0$–$^5G_{2–6}$ at 383 nm, $^7F_0$–$^5L_6$ at 395 nm, $^7F_0$–$^5D_3$ at 416 nm, $^7F_0$–$^5D_2$ at 467 nm and $^7F_0$–$^5D_1$ at 533 nm [38]. These excitation lines in the UV, violet and blue laser diodes/LEDs are efficient pumping sources in obtaining Eu^{3+} emissions. It can be concluded that the nanophosphors obtained in this study can be excited with the intense CTB and moderately intense f–f transitions at 395 nm ($^7F_0$–$^5L_6$) and 467 nm ($^7F_0$–$^5D_2$) are useful for various optoelectronic applications.

The photoluminescent (PL) emission spectra of $Gd_{1.9}Eu_{0.1}O_3$ nanophosphor prepared under different sintering temperatures are shown in Fig. 7. There are five groups of distinctive emission peaks between 550 and 720 nm in the spectra, related to the electronic transitions from the excited $^5D_0$ to ^7F_J (J=0, 1, 2, 3, and 4) levels of Eu^{3+} ions [39,40] and are assigned to $^5D_0$–$^7F_0$ (581 nm), $^5D_0$–$^7F_1$ (588, 593, and 599 nm), $^5D_0$–$^7F_2$ (612, and 630 nm), $^5D_0$–$^7F_3$ (651 nm) and $^5D_0$–$^7F_4$ (707 nm) transitions. The intensities of transitions between different J levels depend on the symmetry of the local environment of Eu^{3+} activators and can be deduced in terms of the Judd–Ofelt theory [41]. If Eu^{3+} is located in a site with an inversion centre, the $^5D_0$–$^7F_1$ magnetic dipole transition should be dominant, while in a site without an inversion centre, the $^5D_0$–$^7F_2$ electric dipole transition will be predominant. The intense peak at 612 nm corresponds to the hypersensitive forced electric dipole $^5D_0$–$^7F_2$ transition of Eu^{3+} ion with the selection rule ΔJ=2 [5], induced by the lack of inversion symmetry. Rare earth ions gives sharp line output due to the transitions within the 4f shell, which is shielded from environmental effects by the outer shell electrons, and are forbidden, but allowed due to the surrounding crystal field relaxing the selection rules.

In cubic Gd_2O_3 lattice, Eu^{3+} ions are occupying two sites: one is the 24d-site with C_2 point non-inversion symmetry and another is the 8b-site with S_6 point inversion symmetry and the ratio between them is 3:1 and both these sites are reflected in the spectral properties as seen in Fig. 7. The $^5D_0$–$^7F_2$ transition of Eu^{3+} ions in sites with S_6 symmetry is strictly forbidden due to the inversion symmetry [42]. The $^5D_0$–$^7F_1$ orange emission dominates when Eu^{3+} ions occupy sites with inversion symmetry (S_6). The observed profound $^5D_0$–$^7F_2$ emission at 612 nm comes from the Eu^{3+} ions preferably occupying the C_2 sites with non-inversion symmetry, which in turn indicates increase in colour purity. From Fig. 8, it can be seen that the integrated photoluminescence intensity is found to increase with sintering temperature up to 800 °C and beyond that no significant increase in intensity was observed. The low emission intensity of the samples prepared at lower sintering temperature may be due to incomplete phase formation and presence of other organic impurities, which may act as quenchers of luminescence and deteriorate their properties. Fig. 9 shows the dependence of integrated emission intensities of $^5D_0$–$^7F_2$ and $^5D_0$–$^7F_1$ transitions of $Gd_{1.9}Eu_{0.1}O_3$ nanophosphors as a function of sintering temperature. Intensity of photoemission of both transitions increases with increase of temperature up to 800 °C. Emission intensities may depend on grain size, homogeneity of doping, activation between host and activator, crystallinity and lesser surface defects and quenching centres. In order to further characterize luminescent properties, the asymmetric ratio (A) [5] is calculated for $^5D_0$–$^7F_2$ and

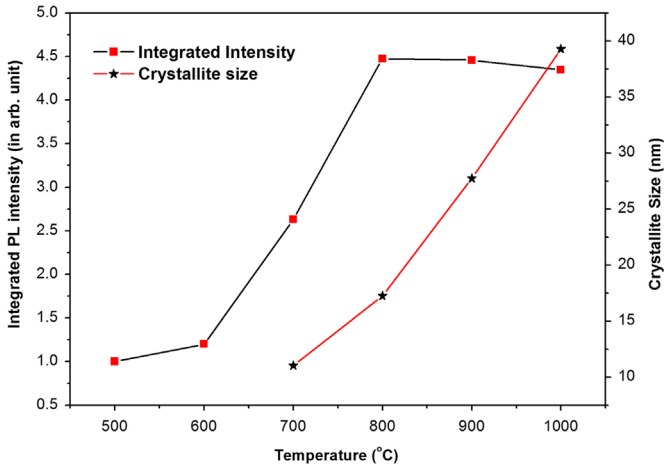

Fig. 8. Variation of grain size and the integrated emission intensity of $Gd_{1.9}Eu_{0.1}O_3$ nanophosphor (λ_{ex}=265 nm) samples sintered at different temperatures.

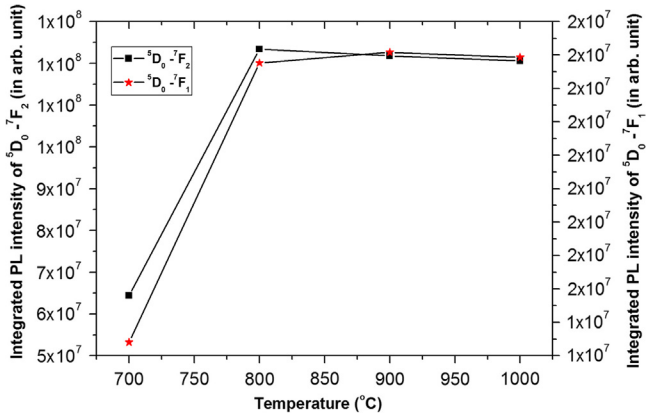

Fig. 9. Dependence of emission intensity of $^5D_0$–$^7F_2$ electric dipole transition and $^5D_0$–$^7F_1$ magnetic dipole transition of $Gd_{1.9}Eu_{0.1}O_3$ nanophosphors sintered at different temperatures.

$^5D_0$–$^7F_1$ transitions as

$$\text{Asymmetric ratio } (A) = \frac{\int I(^5D_0 - {}^7F_2)}{\int I(^5D_0 - {}^7F_1)} \tag{6}$$

The dependence of asymmetric ratio on the sintering temperature under CTB excitation at 265 nm is shown in Fig. 10. An asymmetric factor greater than 1 indicates a highly asymmetric environment (from centre of inversion) around the metal ion. This ratio can be considered as an indicator of the asymmetry of the coordination polyhedron of the Eu^{3+} ion [43]. It can be seen that the asymmetric ratio obtained in this study for samples sintered at 800 °C is around 5.669 and it indicates the high asymmetric environment around the metal ion in the sample.

Commission Internationale de L'Eclairage (CIE) in 1931 developed a set of three colour matching functions ($\bar{x}(\lambda)$, $\bar{y}(\lambda)$, and $\bar{z}(\lambda)$) corresponding to red, green and blue for a 2 degree observer to produce the full range of monochromatic colours. By using the colour matching functions, light stimuli having any spectral power distribution could be specified for colour by

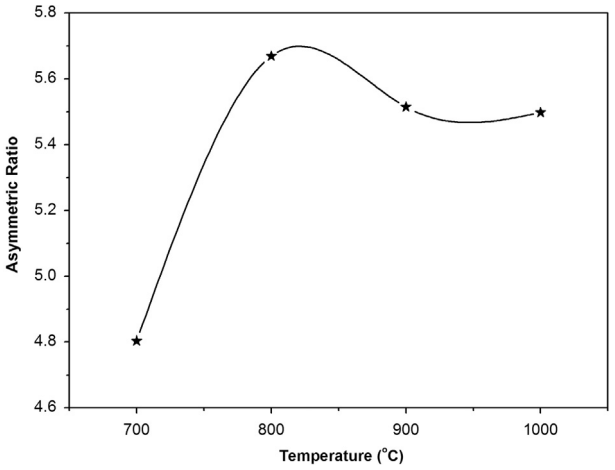

Fig. 10. Variation of asymmetric ratio of $Gd_{1.9}Eu_{0.1}O_3$ nanophosphor with sintering temperature (λ_{ex}=265 nm).

the three (X, Y and Z) values as

$$X = \int_{\lambda} I(\lambda)\bar{x}(\lambda)d\lambda \tag{7}$$

$$Y = \int_{\lambda} I(\lambda)\bar{y}(\lambda)d\lambda \tag{8}$$

$$Z = \int_{\lambda} I(\lambda)\bar{z}(\lambda)d\lambda \tag{9}$$

where $I(\lambda)$ is the spectral distribution of light stimulus. These integrated values (X, Y, and Z) are called Tristimulus values. By projecting the tristimulus values on to the unit plane ($X+Y+Z=1$), colour can be expressed in a two dimensional plane, called the chromaticity diagram. Thus, the colour can be specified by the chromaticity coordinates (x, y) defined by

$$x = \frac{X}{(X+Y+Z)} \tag{10}$$

$$y = \frac{Y}{(X+Y+Z)} \tag{11}$$

The diagram using the chromaticity coordinates (x, y) is referred to as the CIE 1931 chromaticity diagram, or the CIE (x, y) chromaticity diagram [44]. Table 2 lists the CIE colour chromaticity coordinates derived from the emission spectra of $Gd_{1.9}Eu_{0.1}O_3$ nanophosphor prepared at various sintering temperatures and the corresponding coordinates were marked on the 1931 CIE chromaticity diagram and is shown in Fig. 11. For samples prepared at and above 700 °C, the CIE coordinates remain almost the same and are very close to the standard red colour region of the diagram. Colour temperature has been used as a metric to characterize broad band light sources. For broadband light sources that do not produce light from a heated element, their colour temperature can be characterized by Correlated Colour Temperature (CCT), measured in Kelvin (K). CCT is the temperature of a blackbody radiator whose chromaticity point is closest to the chromaticity point of the non-planckian light source. The CCT of the phosphor samples

Table 2
CIE chromaticity coordinates (x, y) and correlated colour temperature (CCT) obtained from the emission spectra of $Gd_{1.9}Eu_{0.1}O_3$ samples sintered at different temperatures.

Sample	Temperature (°C)	CIE coordinates		CCT (K)
		x	y	
a	500	0.5579	0.3545	1626
b	600	0.5581	0.3484	1641
c	700	0.6052	0.3488	1872
d	800	0.6341	0.3530	2052
e	900	0.6201	0.3498	1986
f	1000	0.6180	0.3489	1973

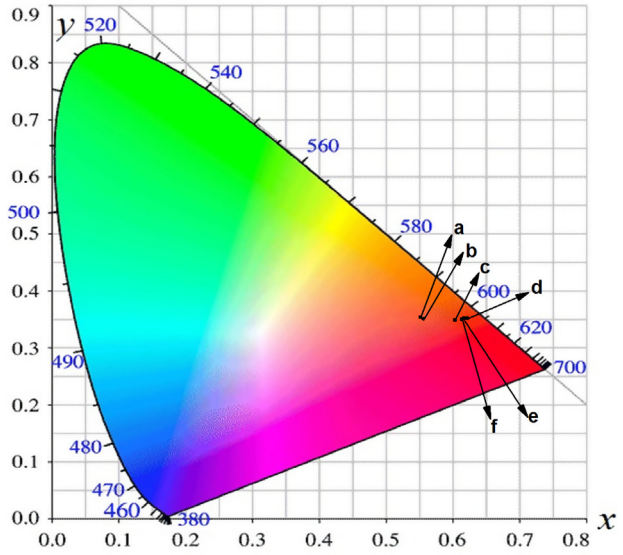

Fig. 11. CIE chromaticity diagram showing the coordinates for the emission spectra of $Gd_{1.9}Eu_{0.1}O_3$ nanophosphor synthesized at different temperatures (a) 500, (b) 600, (c) 700, (d) 800, (e) 900 and (f) 1000 °C.

was calculated according to the method proposed by McCamy [45] and is summarized in Table 2.

In general, decay kinetics behaviour depends on the number of luminescent centres, energy transfer, defects, and impurities in the host. Photoluminescence decay lifetime data were monitored and analyzed for the $^5D_0$–$^7F_2$ transition at 612 nm and is shown in Fig. 12. The experimental decay profile can be fitted well by a single exponential function given by

$$I(t) = I_0 \exp\left(-\frac{t}{\tau}\right) \tag{12}$$

where I_0 is the initial emission intensity at $t=0$ and τ is the lifetime of the emission centre. The lifetimes obtained for the $^5D_0$ lowest excited state is shown in Fig. 12 and are consistent with the reported values for other Eu^{3+} doped Gd_2O_3 systems [46,15]. The decay curves can be fitted with an exponential decay function of first order, which shows that there is one emission centre present in the host lattice. The increase in lifetime with sintering temperature can be attributed to the improvement of crystallinity, grain size and lesser density of defects in the nanoparticles.

The Judd–Ofelt theory [47,48] is a very useful tool to explain the spectroscopic properties of lanthanide ions in a specific coordination environment. Usually, Judd–Ofelt (J–O) parameters, Ω_λ (λ=2, 4, and 6) are calculated to determine the structural changes surrounding Eu^{3+} due to variations of crystal phases and host lattice. Usually, the Judd–Ofelt intensity parameters are obtained from the absorption spectra. However, in the case of Eu^{3+} ion, the pure magnetic dipole transition $^5D_0$–$^7F_1$ allows the determination of the intensity parameters from the emission spectra. When the lanthanide ion is in a highly symmetric environment, Ω_2 parameter will be low. The Ω_4 and Ω_6 parameters are more sensitive toward macroscopic properties, such as rigidity of the matrix, viscosity, dielectric constant in which lanthanide ion is embedded. In this investigation, J–O parameters and other radiative properties were determined from the emission spectrum. The $^5D_0$–$^7F_1$ of Eu^{3+} ion is a magnetic dipole transition, which is independent of the environment and can be used as a reference. According to the J–O theory, the magnetic dipole transition rate (A_{01}) of $^5D_0$–$^7F_1$ transition of Eu^{3+} ion is

$$A_{01} = \frac{64\pi^4\,\nu_1^3\,n^3 S_{\mathrm{md}}}{3h(2J+1)} \tag{13}$$

The electric dipole transition rates (A_{0J}) of $^5D_0$–^7F_J transition (J=2, 4 and 6) is expressed as

$$A_{0J} = \frac{64\pi^4\,\nu_J^3}{3h(2J+1)} e^2 \frac{n(n^2+2)^2}{9} \sum_{\lambda=2,4,6} \Omega_\lambda \left|\langle {}^5D_0 \| U^{(\lambda)} \| {}^7F_J \rangle\right|^2 \tag{14}$$

where A_{0J} is the coefficient of spontaneous emission, e is the electronic charge, ν_J is the wavenumber of the corresponding transition, ($2J$+1) equals to 1 for $^5D_0$ transitions, h is the Planck's constant, S_{md} refers to the strength of the magnetic dipole $^5D_0$–$^7F_1$ transition, which is a constant and independent of the medium, being equal to 9.6×10^{-42} units [49], and n is the effective refractive index of the nanophosphor sample. $|\langle {}^5D_0 \| U^{(\lambda)} \| {}^7F_J \rangle|^2$ is the squared reduced matrix element whose value is independent of the chemical environment of Eu^{3+} and are 0.00324, 0.00229 and 0.00023 for J=2, 4 and 6 [50], respectively. Since the transition rate of each energy level is in direct proportion to integral intensity of emission spectrum, and hence the ratio of electric dipole transition to magnetic dipole transition rate can be expressed as

$$\frac{\int I_J\, d\nu}{\int I_1\, d\nu} = \frac{A_{0J}}{A_{01}} = \frac{e^2}{S_{\mathrm{md}}} \frac{\nu_J^3}{\nu_1^3} \frac{(n^2+2)^2}{9n^2} \Omega_\lambda \left|\langle {}^5D_0 \| U^{(\lambda)} \| {}^7F_J \rangle\right|^2 \tag{15}$$

and hence Ω_2, Ω_4 and Ω_6 can be calculated. The emission of $^5D_0$–$^7F_6$ transition locates in the infrared region and was quite weak, which could not be experimentally detected here, hence Ω_6 not estimated in this case.

The observed fluorescence lifetime τ_{obs} of $^5D_0$, radiative transition rate A_R and non-radiative transition rate A_{NR} can be

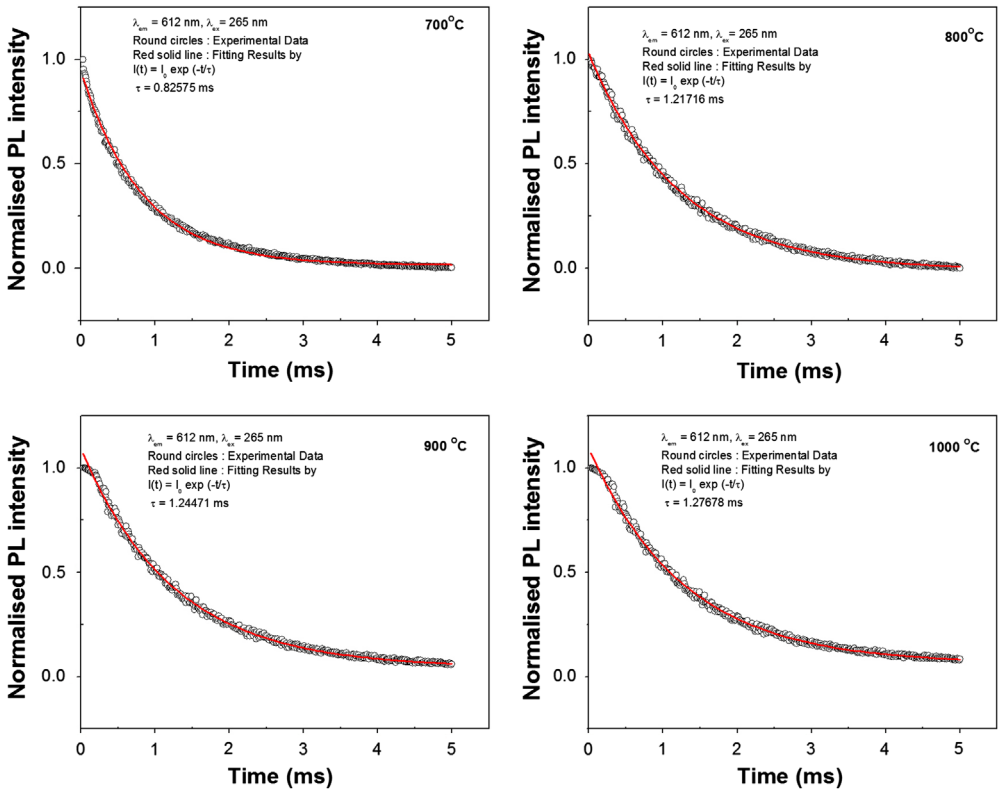

Fig. 12. Room temperature luminescent decay curves of $^5D_0$–$^7F_2$ transition at 612 nm for Eu^{3+} ions in $Gd_{1.9}Eu_{0.1}O_3$ nanophosphors.

expressed as

$$\frac{1}{\tau_{obs}} = A_T = A_R + A_{NR} \tag{16}$$

where A_T is the total transition rate.

The total radiative transition probability (A_R) can be obtained by summing over the radiative rates A_{0J} for each $^5D_0$–^7F_J transition and is given by

$$A_R = \sum_J A_{0J} = A_{01}\frac{\nu_{01}}{I_{01}}\sum_{J=0}^{4}\frac{I_{0J}}{\nu_{0J}} \tag{17}$$

where ν_{01} and ν_{0J} are the energy barycentres of the $^5D_0$–$^7F_1$ and $^5D_0$–^7F_J transitions, A_{01} is the Einstein's coefficient between $^5D_0$–$^7F_1$ levels, and I_{0J} is the integrated area related to the corresponding $^5D_0$–^7F_J transition obtained from the PL spectral data.

As the coefficients for spontaneous emission equal the reciprocal of the radiative relaxation time (τ_{rad})

$$\tau_{rad} = \frac{1}{\sum A_{0J}} = \frac{1}{A_R} \tag{18}$$

Further, quantum efficiency is expressed as the ratio of the number of photons emitted by Eu^{3+} to that of photons absorbed by Eu^{3+} and it is a balance between radiative and non-radiative processes. With the measured lifetime τ_{obs}, together with the above calculated radiative lifetime τ_{rad}, the luminescence quantum yield, η can be calculated using

$$\eta = \frac{\tau_{obs}}{\tau_{rad}} = \frac{A_R}{A_R + A_{NR}} \tag{19}$$

The variations in intensity of emission lines indicate certain selection rules, which in turn decide the branching ratio. The branching ratio measures the percentage of emission for a given transition from a state with respect to all other transitions from this state. The relative amplitudes of the fluorescence transitions or fluorescence branching ratio (β_{0J}) is calculated by

$$\beta_{0J} = \frac{A_{0J}}{\sum A_{0J}} \tag{20}$$

Another radiative property to be evaluated is the stimulated emission cross-section (σ_{0J}) which can be calculated using

$$\sigma_{0J} = \frac{\lambda_p^4}{8\pi c n^2\,\Delta\lambda_{eff}}A_{0J} \tag{21}$$

where λ_p is the wavelength of peak emission (in nm) and $\Delta\lambda_{eff}$ is the effective line width of the emission band.

Table 3 presents the Judd–Ofelt intensity parameters of the samples together with the emission intensity ratios of the transitions from the $^5D_0$ level of Eu^{3+} to ^7F_J multiplets. According to the Judd–Ofelt theory, transitions from the $^5D_0$ state to low-lying ^7F_J levels with $J=0$, 3 or 5 are both electrically and magnetically forbidden. However the observed weak transitions from $^5D_0$ to these levels in the emission spectrum may be due to the crystal field induced J-mixing effect [50]. The R_{02} intensity parameter (see Table 3), defined as the ratio between the intensities of the $^5D_0$–$^7F_0$ and $^5D_0$–$^7F_2$ transitions, gives information about the J-mixing effect associated with the $^5D_0$–$^7F_0$ transition. This effect is mainly due to the mixing between the $^7F_2$ manifold and the $^7F_0$ level, through

Table 3
Judd–Ofelt intensity parameters (Ω_2, and Ω_4) and ratio of integrated emission intensities of the $^5D_0$–$^7F_0$ and $^5D_0$–$^7F_2$ (R_{02}), $^5D_0$–$^7F_2$ and $^5D_0$–$^7F_1$ (R_{21}), $^5D_0$–$^7F_4$ and $^5D_0$–$^7F_1$ (R_{41}) for the transitions from $^5D_0$ to the ^7F_J multiplets determined from emission spectra of $Gd_{1.9}Eu_{0.1}O_3$ samples sintered at different temperatures.

Temperature (°C)	No J mixing		J mixing		R_{02}	R_{21}	R_{41}
	Ω_2 ($\times 10^{-20}$ cm^2)	Ω_4 ($\times 10^{-20}$ cm^2)	Ω_2 ($\times 10^{-20}$ cm^2)	Ω_4 ($\times 10^{-20}$ cm^2)			
700	6.9348	0.8501	8.0246	0.9497	0.0243	4.8035	0.2700
800	8.5140	1.2775	9.8520	1.4271	0.0323	5.66943	0.3900
900	8.3069	1.2569	9.6123	1.4041	0.0341	5.51487	0.3825
1000	8.3097	1.2111	9.6156	1.3529	0.0316	5.49839	0.3674

Table 4
Transition rates (A_R, A_{NR}, and A_T), life time (τ_{rad}, and τ_{obs}), quantum efficiency (η), branching ratios (β_{01}, β_{02}, and β_{04}) and stimulated emission cross-sections (σ_{01}, σ_{02}, and σ_{04}) of the $Gd_{1.9}Eu_{0.1}O_3$ nanophosphors determined from the emission spectra and life time data.

Radiative parameter	Temperature (°C)			
	700	800	900	1000
A_R (s^{-1})	682.55	646.01	620.86	602.50
A_{NR} (s^{-1})	528.47	175.57	182.54	180.72
A_T (s^{-1})	1211.02	821.58	803.40	783.22
τ_{rad} (ms)	1.46509	1.54796	1.61066	1.65975
τ_{obs} (ms)	0.82575	1.21716	1.24471	1.27678
η (%)	56.36	78.63	77.28	76.93
β_{01} (%)	15.325	13.008	13.275	13.381
β_{02} (%)	75.976	76.113	75.556	75.932
β_{04} (%)	4.933	6.048	6.055	5.861
σ_{01} (cm^2)	5.2425×10^{-22}	7.4297×10^{-22}	7.5050×10^{-22}	6.9334×10^{-22}
σ_{02} (cm^2)	3.6275×10^{-21}	3.9801×10^{-21}	3.8690×10^{-21}	3.8291×10^{-21}
σ_{04} (cm^2)	4.0941×10^{-22}	5.9459×10^{-22}	5.8613×10^{-22}	5.4500×10^{-22}

the rank two components of the ligand field. The obtained values of J–O parameters are in consistent with the reported values obtained [50]. The larger value of the Ω_2 parameter reflects the hypersensitive behaviour of the $^5D_0$–$^7F_2$ transition and indicates that Eu^{3+} ions are located in a higher polarizable chemical environment. Ω_2 is expected to increase with decrease in site symmetry, an increase in coordination number and a decrease in bond length. Transition rates (A_R, A_{NR}, and A_T), life time (τ_{rad}, and τ_{obs}), quantum efficiency (η), branching ratios (β_{01}, β_{02}, and β_{04}) and stimulated emission cross-sections (σ_{01}, σ_{02}, and σ_{04}) of the $Gd_{1.9}Eu_{0.1}O_3$ nanophosphors determined from the emission spectra and life time data are given in Table 4. From the table, it can be seen that the phosphors synthesized above 700 °C maintained a quantum efficiency of more than 75%. The emission cross-section (σ_{02}) associated with the $^5D_0$–$^7F_2$ electronic transition is larger, showing more colour purity and lower symmetry of Eu^{3+} ions. The $^5D_0$–$^7F_2$ (612 nm) transition is highly sensitive to structural, morphological and environment changes and may affect the symmetry of crystal fields around Eu^{3+} ions lowering the symmetry of cation sites resulting in enhanced emission. In short, activation of Eu^{3+} in host matrix, grain size, defects and crystallinity may also affect luminescence intensity of the phosphor samples.

4. Conclusions

$Gd_{1.9}Eu_{0.1}O_3$ nanophosphor was synthesized by controlled combustion of metal–citrate complex in the Diethylene glycol medium. Phase formation is achieved at a relatively low temperature and their optical and luminescent properties were evaluated. Structure and morphology of the samples were investigated using X-ray diffraction, Raman spectroscopy and TEM measurements. The samples prepared by sintering at 800 °C were nanocrystalline with a lattice spacing of 0.312 nm, of cubic Gd_2O_3 and showed high degree of homogeneity, a maximum quantum efficiency of 78% and life time of 1.22 ms. Excitation spectra confirmed the efficient energy transfer between Gd^{3+} and Eu^{3+} ions and the emission spectra showed rich red emission at 612 nm, leading to better colour purity. CIE coordinates were evaluated and found to be close to the standard red colour. The luminescence decay curves were well fitted by a single exponential function and the lifetime is found to increase with sintering temperature. The Judd–Ofelt intensity parameters, transition rates, branching ratios, quantum efficiency and emission cross-sections were calculated from the emission spectrum and using the J–O theory. The results obtained are fruitful and will provide a basis for the design of efficient red phosphors for display, lighting and in medical applications. The synthesis method adopted here offers a feasible and cost effective

technique for the preparation of a variety of phosphor materials for optoelectronic applications.

Acknowledgment

R.G. Abhilash Kumar acknowledges University Grants Commission (UGC), India, for the award of teacher fellowship under the Faculty Development Programme.

References

[1] H. Tuller, Solid state electrochemical systems-opportunities for nanofabricated or nanostructured materials, Journal of Electroceramics 1 (3) (1997) 211–218.
[2] P.D. Rack, P.H. Holloway, The structure, device physics and material properties of thin film electroluminescent displays, Materials Science and Engineering:R:Reports 21 (4) (1998) 171–219.
[3] R.C. Ropp, Luminescence and the Solid State, Second ed., Elsevier Science Publishers B.V., Amsterdam, 2004.
[4] A.J. Kenyon, Recent developments in rare earth doped materials for optoelectronics, Progress in Quantum Electronics 26 (2002) 225–284.
[5] G. Blasse, B.C. Grabmaier, Luminescent Materials, Springer-Verlag, Berlin, 1994.
[6] M. Nichkova, D. Dosev, S.J. Gee, B.D. Hammock, I.M. Kennedy, Microarray immunoassay for phenoxybenzoic acid using polymer encapsulated Eu:Gd_2O_3 nanoparticles as fluorescent labels, Analytical Chemistry 77 (2005) 6864–6873.
[7] M. Nichkova, D. Dosev, R. Perron, S.J. Gee, B.D. Hammock, I.M. Kennedy, Eu^{3+} doped Gd_2O_3 nanoparticles as reporters for optical detection and visualization of antibodies patterned by microcontact printing, Analytical and Bioanalytical Chemistry 384 (2006) 631–637.
[8] B. Vinila, P.D. Dimple, M. Mohapatra, S.V. Godbole, R. Ghildiyal, A.K. Tyagi, Rare-earth doped gadolinia based phosphors for potential multicolor and white light emitting deep UV LEDs, Nanotechnology 20 (2009) 125707.
[9] S.C. Sun, B. Murray, Synthesis of monodisperse cobalt nanocrystals and their assembly into magnetic superlattices, Journal of Applied Physics 85 (1999) 4325–4330.
[10] E. Zych, C. Brecher, A.J. Wojtowicz, H. Lingertat, Luminescence properties of Ce-activated YAG optical ceramic scintillator materials, Journal of Luminescence 75 (1997) 193–203.
[11] J. Yang, C. Li, Z. Quan, C. Zhang, P. Yang, Y. Li, C. Yu, J. Lin, Self-assembled 3D flowerlike Lu_2O_3 and Lu_2O_3:Ln^{3+} (Ln=Eu, Tb, Dy, Pr, Sm, Er, Ho, Tm) microarchitecture:ethylene glycol mediated hydrothermal synthesis and luminescent properties, Journal of Physical Chemistry C 112 (2008) 12777–12785.
[12] S. Li, H. Song, H. Yu, S. Lu, X. Bai, G. Pan, Y. Lei, L. Fan, T. Wang, Influence of annealing temperature on photoluminescence characteristics of Gd_2O_3:Eu/AAO nanowires, Journal of Luminescence (122–123) (2006) 876–878.
[13] S. Seo, H. Yang, P.H. Holloway, Controlled shape growth of Eu or Tb-doped luminescent Gd_2O_3 colloidal nanocrystals, Journal of Colloid and Interface Science 331 (2009) 236–242.
[14] O. Milosevic, L. Mancic, B. Jordovic, R. Maric, S. Ohara, T. Fukui, Processing of Gd_2O_3:Eu phosphor particles through aerosol route, Journal of Materials Processing Technology (143–144) (2003) 501–505.
[15] L. Liu, E. Ma, R. Li, G. Liu, X. Chen, Effects of phonon confinement on the luminescence dynamics of Eu^{3+} in Gd_2O_3 nanotubes, Nanotechnology 18 (2007) 015403.
[16] Y. Li, G. Hong, Synthesis and luminescence properties of nanocrystalline Gd_2O_3:Eu^{3+} by combustion process, Journal of Luminescence 124 (2007) 297–301.
[17] Z. Wang, W. Zhang, L. Lin, B. You, Y. Fu, M. Yin, Preparation and spectroscopic characterization of Lu_2O_3:Eu^{3+} nanopowders and ceramics, Optical Materials 30 (2008) 1484–1488.
[18] M.E. Rabanal, C. Moral, J.M. Torralba, L. Mancic, O. Milosevic, Gd_2O_3:Eu^{3+} phosphor particles processed through aerosol route, Journal of the European Ceramic Society 25 (2005) 2023–2027.
[19] J. Trojan-Piegza, E. Zych, Preparation of nanocrystalline Lu_2O_3:Eu phosphor via a molten salts route, Journal of Alloys and Compounds 380 (2004) 118–122.
[20] G. Jia, H. You, K. Liu, Y. Zheng, N. Guo, H. Zhang, Highly uniform Gd_2O_3 hollow microspheres: template directed synthesis and luminescent properties, Langmuir 26 (7) (2010) 5122–5128.
[21] Y.C. Kang, H.S. Roh, S.B. Park, H.D. Park, Use of LiCl flux in the preparation of Y_2O_3:Eu phosphor particles by spray pyrolysis, Journal of the European Ceramic Society 22 (2002) 1661–1665.
[22] Geo Rajan, K.G. Gopchandran, Enhanced luminescence from spontaneously ordered Gd_2O_3:Eu^{3+} based nanostructures, Applied Surface Science 255 (2009) 9112–9123.
[23] W.N. Wang, W. Widiyastuti, T. Ogi, I.W. Lenggoro, K. Okuyama, Correlations between crystallite/particle size and photoluminescence properties of submicrometer phosphors, Chemistry of Materials 19 (2007) 1723–1730.
[24] A.E. Morales, E.S. Mora, U. Pal, Use of diffuse reflectance spectroscopy for optical characterization of unsupported nanostructures, Revista Mexicana de Fisica S53 (5) (2007) 18–22.
[25] R. Sanchez Zeferino, U. Pal, R. Melendrez, H.A. Duran-Munoz, M. Barboza Flores, Dose enhancing behavior of hydrothermally grown Eu-doped SnO_2 nanoparticles, Journal of Applied Physics 113 (2013) 064306.
[26] E. Matijevic, W.P. Hsu, Preparation and properties of monodispersed colloidal particles of lanthanide compounds: I. Gadolinium, europium, terbium, samarium, and cerium(III), Journal of Colloid and Interface Science 118 (1987) 506–523.
[27] K. Nakamoto, Infrared and Raman Spectra of Inorganic and Coordination Compounds, Sixth ed., John Wiley & Sons, New Jersey, 2009.
[28] T. Gougousi, D. Niu, R.W. Ashcraft, G.N. Parsons, Carbonate formation during post-deposition ambient exposure of high-k dielectrics, Applied Physics Letters 83 (2003) 3543–3545.
[29] A. Garcia-Murillo, C.L. Luyer, C. Dujardin, C. Pedrini, J. Mugnier, Elaboration and characterization of Gd_2O_3 waveguiding thin films prepared by the sol–gel process, Optical Materials 16 (2001) 39–46.
[30] R.G. Haire, L. Eyring, Comparisons of the binary oxides, in: K.A. Gschneidner Jr., L. Eyring, G.R. Choppin, G.H. Lander (Eds.), Handbook on the Physics and Chemistry of Rare Earths, 18, Elsevier Science Publishers B.V., Amsterdam, 1994, pp. 413–505.
[31] Y. Repelin, C. Proust, E. Husson, J.M. Beny, Vibrational spectroscopy of the c-form of yttrium sesquioxide, Journal of Solid State Chemistry 118 (1995) 163–169.
[32] W.B. White, V.G. Keramidas, Vibrational spectra of oxides with the c-type rare earth oxide structure, Spectrochimica Acta A 28 (1972) 501–509.
[33] C.L. Layer, A. Garcia-Murillo, E. Bernstein, J. Mugnier, Waveguide raman spectroscopy of sol–gel Gd_2O_3 thin films, Journal of Raman Spectroscopy 34 (2003) 234–239.
[34] L. Li, S.Y. Zhang, Dependence of charge transfer energy on crystal structure and composition in Eu^{3+}-doped compounds, Journal of Physical Chemistry B 110 (2006) 21438–21443.
[35] L. Li, H.K. Yang, B.K. Moon, B.C. Choi, J.H. Jeong, K.H. Kim, Photoluminescent properties of Ln_2O_3:Eu^{3+} (Ln=Y, Lu and Gd) prepared by hydrothermal process and sol–gel method, Materials Chemistry and Physics 119 (2010) 471–477.
[36] C. Wu, W. Qin, G. Qin, D. Zhao, J. Zhang, S. Huang, S. Lu, H. Liu, H. Lin, Photoluminescence from surfactant-assembled Y_2O_3:Eu nanotubes, Applied Physics Letters 82 (2003) 520–522.
[37] G.Z. Li, M. Yu, Z.L. Wang, J. Lin, R.S. Wang, J. Fang, Sol–gel fabrication and photoluminescence properties of SiO_2@Gd_2O_3:Eu^{3+} core–shell particles, Journal of Nanoscience and Nanotechnology 6 (2006) 1416–1422.
[38] J. Yang, C. Li, Z. Cheng, X. Zhang, Z. Quan, C. Zhang, J. Lin, Size-tailored synthesis and luminescent properties of one-dimensional Gd_2O_3:Eu^{3+} nanorods and microrods, Journal of Physical Chemistry C 111 (2007) 18148–18154.

[39] L. Xu, B. Wei, Z. Zhang, Z. Lu, H. Gao, Y. Zhang, Synthesis and luminescence of europium doped yttria nanophosphors via a sucrose-templated combustion method, Nanotechnology 17 (2006) 4327–4331.
[40] T. Kushida, M. Tanaka, Transition mechanisms and spectral shapes of the $^5D_0$–$^7F_0$ line of Eu^{3+} and Sm^{2+} in solids, Physical Review B 65 (2002) 195118.
[41] L. Xu, X.Y. Yang, Z. Zhai, X. Chao, Z.H. Zhang, W.H. Hou, EDTA-mediated hydrothermal synthesis of $NaEu(MoO_4)_2$ microrugbies with tunable size and enhanced luminescence properties, CrystEngComm 13 (2011) 4921–4929.
[42] C.X. Liu, J.Y. Liu, K. Dou, Judd–Ofelt intensity parameters and spectral properties of Gd_2O_3:Eu^{3+} nanocrystals, Journal of Physical Chemistry B 110 (2006) 20277–20281.
[43] E.W.J.L. Oomen, A.M.A. Dongen, Europium (III) in oxide glasses: dependence of the emission spectrum upon glass composition, Journal of Non-Crystalline Solids 111 (1989) 205–213.
[44] R.W.G. Hunt, Measuring Colour: Applied Science and Industrial Technology, Second ed., Ellis Horwood, New York, 1991.
[45] C.S. McCamy, Correlated color temperature as an explicit function of chromaticity coordinates, Color Research and Application 17 (1992) 142–144.
[46] G. Liu, G. Hong, J. Wang, X. Dong, Hydrothermal synthesis of spherical and hollow Gd_2O_3:Eu^{3+} phosphors, Journal of Alloys and Compounds 432 (2007) 200–204.
[47] B.R. Judd, Optical absorption intensities of rare-earth ions, Physical Review 127 (1962) 750–761.
[48] G.S. Ofelt, Intensities of crystal spectra of rare-earth ions, Journal of Chemical Physics 37 (1962) 511–520.
[49] M.J. Weber, T.E. Varitimos, B.H. Matsinger, Optical intensities of rare-earth ions in yttrium orthoaluminate, Physical Review B 8 (1973) 47–53.
[50] L. Liu, X. Chen, Energy levels, fluorescence lifetime and Judd–Ofelt parameters of Eu^{3+} in Gd_2O_3 nanocrystals, Nanotechnology 18 (2007) 255704.